PAPER

Check for updates

Oxidation and Degradation of WS$_2$ Monolayers Grown by NaCl-Assisted Chemical Vapor Deposition: Mechanism and Prevention†

Yao-Pang Chang,[a] Wei-Bang Li,[b,c] Yueh-Chiang Yang,[a] Hsueh-Lung Lu,[a] Ming-Fa Lin,[c] Po-Wen Chiu*[a] and Kuang-I Lin ⓘD *[b]

The preservation of two-dimensional WS$_2$ in the environment is a concern for researchers. In addition to water vapor and oxygen, the latest research points out that degradation is directly related to light absorption. Based on the selection rules of nonlinear optics, two-photon absorption is dipole forbidden in the exciton 1s states, but second-harmonic generation (SHG) is allowed with virtual transitions. According to this mechanism, we proved that SHG is an optical detection method with non-photooxidative damage and energy characteristics. With this detection method, we can explore the oxidation and degradation mechanisms of WS$_2$ grown by NaCl-assisted chemical vapor deposition in its original state. The WS$_2$ monolayers that use NaCl to assist in growth have undergone different degradation processes, starting to oxidize from random positions in the triangular flake. We use a photocatalytic reaction to explain the photo-induced degradation mechanism with sulfur vacancies. It was further found that WS$_2$ grown with NaCl assistance is hydrolyzed in a dark and high-humidity environment, which does not occur in pure WS$_2$. Finally, we demonstrated that changing the direction of the sapphire substrate relative to the gas flow direction to grow NaCl-assisted WS$_2$ can greatly improve its stability in the ambient atmosphere, even when exposed to light. The optimal geometric structures and ground state energies are investigated by the density functional theory-based calculations. According to the orientation and symmetry of NaCl-assisted WS$_2$, we can expect that it will have a better growth quality when the gas flow direction is perpendicular to the [11$\bar{2}$0] direction of the sapphire substrate. This contributes to the nucleation and subsequent growth of NaCl-assisted WS$_2$. This research provides a more stable optical inspection method than other established methods and greatly improves the operational stability of NaCl-assisted WS$_2$ under environmental conditions.

[a]Department of Electrical Engineering, National Tsing Hua University, Hsinchu 30013, Taiwan. E-mail: pwchiu@ee.nthu.edu.tw
[b]Core Facility Center, National Cheng Kung University, Tainan 70101, Taiwan. E-mail: kilin@mail.ncku.edu.tw
[c]Department of Physics, National Cheng Kung University, Tainan 70101, Taiwan
†Electronic supplementary information (ESI) available: Additional information regarding SEM images, schematic diagram of NaCl-assisted CVD, SHG images, PL and Raman spectra, AFM measurements, EDS analyses, and WS$_2$ size analysis. See DOI: 10.1039/d1nr04809k

The excellent properties of two-dimensional (2D) transition metal dichalcogenide (TMD) materials result in their widespread use in supercapacitors,[1] electrocatalysts,[2] photovoltaics,[3] photocatalysts,[4–6] optoelectronic devices,[7] environmental gas sensors,[8] *etc.*, but these applications require the stability of the materials in the environment. However, TMD materials are not as stable as they had been thought. A variety of surface defects in TMD has been reviewed and classified as zero-, one- and two-dimensional defects, which have a large impact on their electrical and optical properties.[9–11] The defects can come from the material's synthesis, such as chemical vapor deposition (CVD) or chemical vapor transport fabrication,[9,12] as well as post-production stages, *i.e.* electron beam irradiation,[13,14] thermal annealing,[15,16] and laser illumination.[17,18]

Tungsten disulfide (WS$_2$) is one of the most intensively studied layered materials in the TMD family because of its superior properties. Compared with other TMD materials, WS$_2$ possesses a high carrier mobility,[19] large spin–orbit coupling,[20] and a higher photoluminescence (PL).[21] Unfortunately, monolayer WS$_2$ has been shown to degrade over time even at room temperature. After only one month, the transistor device current dropped by nearly two orders of magnitude.[15] Recently, Kotsakidis *et al.*[22] have determined that the oxidation of monolayer WS$_2$ under ambient conditions is a photooxidation process. Oxidation is only observed when the electron

transition is excited. There may be no fluence threshold, and oxidation occurs based on probability, although the detailed mechanism remains to be clarified. Exposure to fluorescent lamps for days (fluence threshold only 1.8×10^6 Jm^{-2}), or exposure to a single PL or Raman spectroscopy measurement, can cause significant oxidative damage. With other methods, such as fluorescence microscopy and laser scanning confocal microscopy (LSCM), the morphology of TMDs can be rapidly obtained, but the energy characteristics of excitons and trions of the sample cannot be obtained.[22,23] In addition, photooxidation in principle cannot be avoided. It is critical to find a fast and convenient optical measurement method, which can absolutely avoid photo-oxidation and detect the energy characteristics. Second-harmonic generation (SHG) can distinguish the exciton resonances as a function of the laser energy, and the related nonlinear optical selection rules.[24–27] Although SHG is a second-order optical process, its intensity at the exciton resonance energy of TMD monolayer can rise to three orders of magnitude.[24] By using nonlinear optical selection rules, we have the opportunity to avoid photooxidation.

Different strategies are adopted to reduce or eliminate the oxidation processes in TMDs, usually using capping layers. These include encapsulation with other monolayer or few-layer materials, such as h-BN,[28] graphene,[29] and pyrene, or use the atomic layer deposition method to cover the material with an oxide layer.[30,31] The capping layer will inevitably affect the intrinsic properties of the TMD and cause inconveniences during the manufacturing process. It is also difficult to remove the capping layer without damaging the TMD. Adding a small amount of alkali metal halides to the growth sources can greatly increase the growth rate of MoS_2 or WS_2, resulting in the rapid formation of large domains.[32–35] In addition, due to the use of sodium halide, the PL intensity of MoS_2 monolayers is greatly increased by about 20–100 times.[35] This is because the deep trap states caused by sulfur vacancies are passivated by the halogen atoms; however, this does not represent the stability of photooxidation. The impact of alkali metal halides on the degradability of TMDs has not yet been established. Moreover, defects are necessary to initiate the oxidation of WS_2 under ambient conditions with light exposure.[22] It has been reported that the lattice structures, step edges, and surface interaction of the sapphire substrate will affect the orientation and properties of TMDs, as well as their thermal stability.[36–39] It is expected that similar methods can be used to reduce defects and thereby improve photooxidation stability. Providing a more stable measurement method and operating stability under environmental conditions for WS_2 is essential for the fundamental research and practical application of WS_2.

In this work, we used characterization tools, including optical microscopy (OM), photoluminescence (PL), Raman spectroscopy, scanning electron microscopy (SEM), atomic force microscopy (AFM), and X-ray photoelectron spectroscopy (XPS) to study pure and NaCl-assisted WS_2 monolayers. Furthermore, we demonstrated a fast, non-photooxidative damage and energy characteristic technology: second-harmonic imaging microscopy. With this technology, we can explore the oxidation and degradation mechanisms of WS_2 in its original state. Although NaCl helps to grow larger WS_2 domains, the NaCl-assisted WS_2 monolayers have undergone different degradation processes, starting to oxidize from random positions in the triangular flakes. We use a photocatalytic reaction to explain the photo-induced oxidation mechanism of monolayer WS_2 with sulfur vacancies. We can conclude that $^\bullet O_2^-$ is the main reactive radical, while $^\bullet OH$ plays a minor role in the photooxidation of WS_2. It was further found that NaCl-assisted WS_2 is hydrolyzed in a dark and high-humidity environment, which does not occur in pure WS_2. The XPS spectra of NaCl-assisted WS_2 samples collected after the degradation process show the presence of Na but no Cl. Finally, we intentionally placed the c-plane sapphire in two orientations with respect to the CVD gas flow to grow NaCl-assisted WS_2 and found that this growth method can greatly improve the stability of WS_2 in the ambient atmosphere, even when exposed to light. The density functional theory (DFT)-based calculations can explain the growth mechanism of WS_2.

Results and discussion

The use of alkali metal halides, such as NaCl and KCl, has allowed the successful growth of large single domain TMD monolayers.[32–35] However, the impact of the alkali metal halides on the degradability of TMDs is not yet established. The following sections aim to focus on the relationship between the NaCl assistant and WS_2 degradation and look for non-photooxidative detection methods. Fig. 1a shows an SEM image of a fresh NaCl assistant WS_2 monolayer. The side length of the triangle reaches 82 μm. The WS_2 flakes grown without NaCl assistant are smaller (see ESI Fig. S1†). This can be contributed by the effort of the NaCl assistant and agrees with other studies.[40,41] Please note that when these WS_2 grow, the sapphire substrates do not choose a specific orientation. The growth related to the substrate orientation to improve photooxidation will be discussed in detail in Fig. 5. Fig. 1b shows the PL spectra of pure and NaCl-assisted WS_2 monolayers. Both display an exciton peak at about 2 eV, but the PL peak of NaCl-assisted WS_2 has a slight blueshift. The PL intensity of NaCl-assisted WS_2 is 1.7 times that of WS_2. This may be similar to the deep trap states of MoS_2 passivated by halogen atoms,[35] but the effect on WS_2 is not as significant as for MoS_2. Fig. 1c shows the Raman spectra of pure and NaCl-assisted WS_2 monolayers. The Raman spectrum is consistent with conventional WS_2, and there is no difference. Preserving 2D WS_2 in the environment is a concern for researchers seeking to avoid TMDs degradation. In addition to water vapor and oxygen, the latest research points out that it is directly related to light absorption, in a process called photooxidation.[22] In the monolayer form, WS_2 is quickly converted into tungsten oxide, WO_x (x ≤ 3), through the reaction, which involves visible wavelength light absorbed by WS_2. Most of the current optical detection methods for 2D materials use PL and Raman spectroscopy. It is difficult to avoid laser damage to the
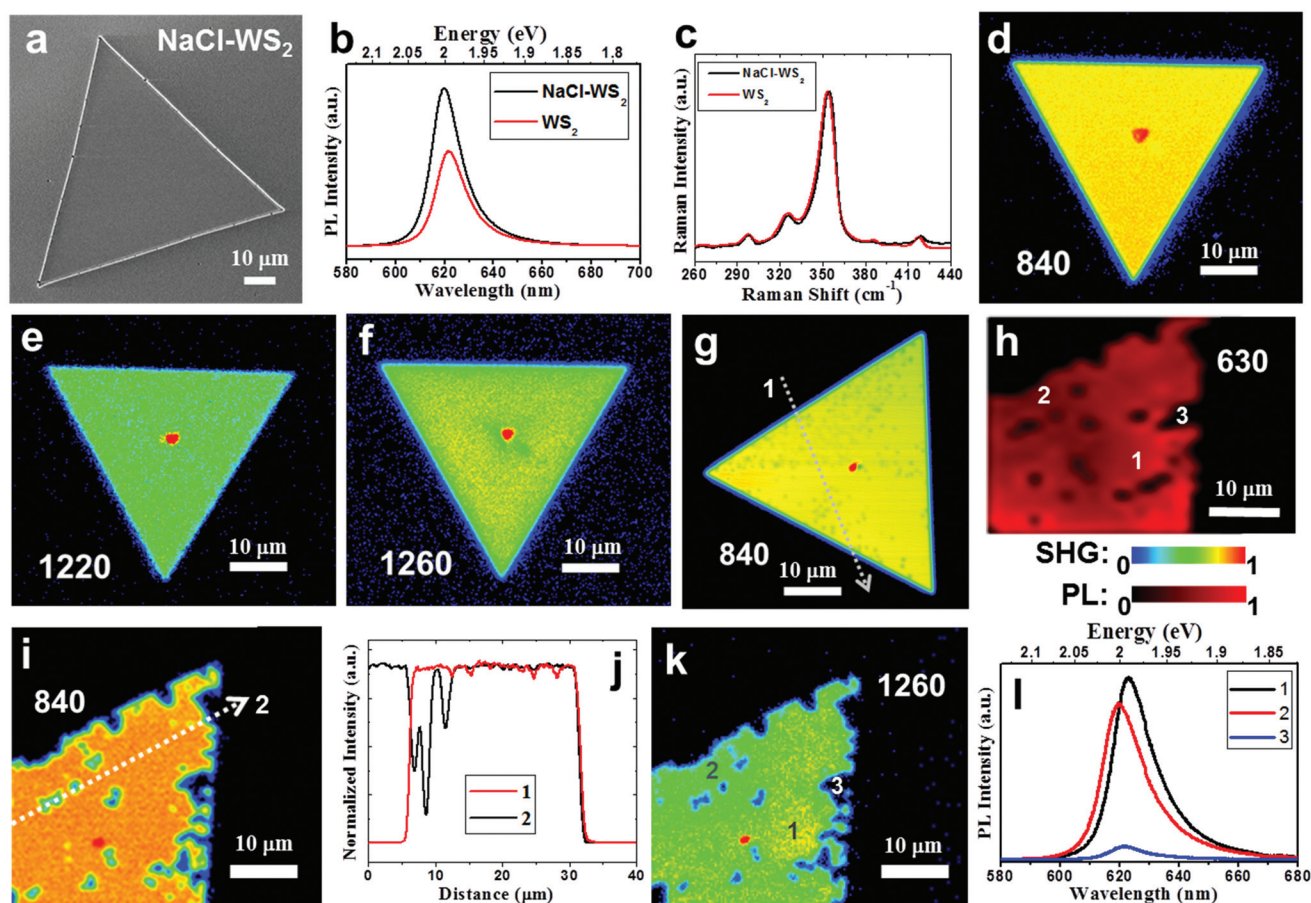
Fig. 1 Sample characterization and demonstration of the non-photooxidative detection capability of SHG. (a) SEM image of a fresh NaCl-assisted WS_2 monolayer. (b) PL spectra of pure and NaCl-assisted WS_2 monolayers. (c) Raman spectra of pure and NaCl-assisted WS_2 monolayers. (d–f) SHG images of a fresh NaCl-assisted WS_2 monolayer excited at 840, 1220, and 1260 nm with fluence of $\sim3.1 \times 10^6$, 4.6×10^7, and 5.1×10^7 Jm^{-2}, respectively. (g) SHG image of a different NaCl-assisted WS_2 monolayer with increased fluence of $\sim6.1 \times 10^8$ Jm^{-2}. (h) PL intensity map of another NaCl-assisted WS_2 monolayer at 630 nm with laser fluence of $\sim1.2 \times 10^9$ Jm^{-2}, which showed obvious degradation. SHG and PL intensity are normalized and shown with a rainbow and red color scale, respectively, and used in the following figures. (i) SHG image of the NaCl-assisted WS_2 monolayer after PL mapping (Fig. 1 h) excited at 840 nm with fluence of $\sim3.1 \times 10^6$ Jm^{-2}. (j) Intensity profiles measured along the white dotted lines in (g, i). (k) SHG image of the NaCl-assisted WS_2 monolayer after PL mapping (Fig. 1 h) excited at 1260 nm with fluence of $\sim5.1 \times 10^7$ Jm^{-2}. (l) Selected PL spectra as marked in (h).

sample, especially for large-area inspections. SHG, a second-order optical nonlinearity, is only dipole-allowed in materials without inversion symmetry.[42,43] Because monolayer WS_2 lacks the inversion symmetry, it has a strong SHG. Here, an in-house built second-harmonic imaging microscope (see Methods) is utilized to demonstrate a fast, non-photooxidative damage, and energy characteristic technology. Fig. 1d–f show SHG images of a fresh NaCl-assisted WS_2 monolayer excited at the fundamental wavelength 840, 1220, and 1260 nm with fluence of $\sim3.1 \times 10^6$, 4.6×10^7, and 5.1×10^7 Jm^{-2}, respectively. These SHG images exhibit a uniform intensity distribution within the single crystal, indicating that there is no photooxidation caused by the laser scanning that produces SHG. The intensity profiles are shown in Fig. S3 (ESI).† This is different from the observation reported by Kotsakidis *et al.*[22] They observed that there is oxidation when fluence is greater than 1.8×10^6 Jm^{-2}. We use the mechanism of SHG to avoid

photooxidation and explain it as follows. The fundamental wavelengths for WS_2 were taken as 1220 and 1260 nm, which are close to half of the energies of excitons and trions of WS_2.[44,45] In contrast to SHG, 1s transitions in two-photon excited photoluminescence (2P-PL) experiments are dipole forbidden at the fundamental excitation wavelengths 1220 and 1260 nm, whose two-photon energy is lower than the 2p exciton state of WS_2.[24,27] Oxidation is only observed upon excitation of a real electronic transition.[22] This allows the use of SHG detection to avoid photooxidation, as shown in Fig. 1e and f.

At 840 nm (see Fig. 1d), the SHG intensity is significantly enhanced by the band nesting energy resonance (C peak).[46] The NaCl-assisted WS_2 monolayer is excited by the corresponding harmonic energy of 2.95 eV, which is higher than the expected low-lying exciton energies of WS_2 monolayers. Under this condition, 2P-PL will be produced, which has a real elec-

tronic transition. We measured a SHG image of a different NaCl-assisted WS$_2$ monolayer excited at 840 nm with increased fluence of ~6.1 × 10^8 Jm^{-2}, which shows faint dark spots as shown in Fig. 1 g. An intensity profile measured along the white dotted line is shown in Fig. 1j. Small dents can be seen in the intensity profile. Furthermore, we produced a PL intensity map of another NaCl-assisted WS$_2$ monolayer at 630 nm with laser fluence of ~1.2 × 10^9 Jm^{-2} (Fig. 1h), which showed obvious degradation. Both laser fluences are more than 300 times larger than the photooxidation threshold of 1.8 × 10^6 Jm^{-2} indicated in ref. 22. It is expected to cause severe photooxidation, but the SHG excited at 840 nm shows only faint dark spots. This is because the probability of two-photon absorption is lower than that of single-photon absorption. The SHG images of the NaCl-assisted WS$_2$ monolayer before the PL mapping is shown in Fig. S4 (ESI),† which do not show any dark spots, indicating that there is no photooxidation during the process of SHG. After the PL mapping, we then measured the SHG excited at 840 nm as shown in Fig. 1i. There are some dark areas and quite consistent with the PL image. The intensity profile shown in Fig. 1j indicates the damage caused by PL. In Fig. 1k, this is the same flake that was used in Fig. 1h and i. The SHG image excited at 1260 nm near the trion resonance shows similar spatial distribution to the PL damage points. In addition, SHG image can also distinguish the spatial distribution of trion in WS$_2$ triangular single crystal after scanning by PL laser. The area marked 1 in Fig. 1k has a strong trion signal. Please refer to the selected PL spectra in Fig. 1l as marked in Fig. 1 h. The red shift of the PL peak represents more trion contributions.[10,23]

After showing that SHG can effectively avoid photooxidation in Fig. 1, we can explore the oxidation and degradation mechanisms of the material in its original state. Now, we discuss the effects that NaCl-assisted WS$_2$ monolayers stored in the environment have and compare them with WS$_2$ monolayers without an NaCl assistant. Fig. 2a shows an SEM image of NaCl-assisted WS$_2$ monolayers stored in a moisture-proof box for 2 months. The humidity condition was 27% RH (relative humidity), and only very weak fluorescent light passed through the box. The irradiance is ~1.7 × 10^{-3} W m^{-2}, which is less than one thousandth of the fluorescence light irradiance. Compared with Fig. 1a, there is no change in the NaCl-assisted WS$_2$ monolayers can be seen in the SEM. Fig. 2b and c show SHG images of the same NaCl-assisted WS$_2$ monolayers shown in Fig. 2a excited at 1220 and 1260 nm, respectively. Unlike fresh NaCl-assisted WS$_2$ shown in Fig. 1e and f, the SHG images have an inhomogeneous distribution. Fig. 2d shows the intensity profiles measured along the white dotted lines in Fig. 2b and c. The intensity profiles show the opposite change, which indicates exciton and trion distributions excited by 1220 and 1260 nm, respectively. Fig. 2e and f show SEM images of a pure WS$_2$ monolayer stored under fluorescent light and 55% RH for 1 day and 7 days, respectively. The pure WS$_2$ monolayer only slightly degrades on the first day as some black dots on the edges, indicated by the dotted circles, show. The WS$_2$ monolayer deteriorated severely on the seventh day. It

started degradation mainly from the edge observed from its SEM image and corresponding to previous studies.[15,18,22,47]

Fig. 2g and h show SEM images of a NaCl-assisted WS$_2$ monolayer stored under fluorescent light and 55% RH for 1 day and 7 days, respectively. SEM images of the NaCl-assisted WS$_2$ monolayer stored for other days are shown in Fig. S5 (ESI).† Interestingly, the NaCl-assisted WS$_2$ monolayer began degradation from random positions in the triangle area. It suffered obvious damage from the 7th day, which can be seen in the SEM image. Raman and PL data collected on the 1st and 7th day are shown in Fig. S6† (ESI). The degradation patterns in the NaCl assistant WS$_2$ are small triangles (see ESI Fig. S7†), which is similar to pure WS$_2$ caused by the surface defects.[10,22,48] The defect positions become weak positions, enabling highly reactive free radicals to attack, followed by degradation. The XPS spectrum of the NaCl-assisted WS$_2$ monolayer was collected in order to understand how severe the light-induced degradation is. The XPS spectrum of the 7th day NaCl-assisted WS$_2$ shows W 4f peaks with Gaussian–Lorentzian fitting in Fig. 2i. The W 4f (WO$_3$) signal appears in the XPS spectrum and has a higher intensity than the W 4f (WS$_2$) peak, which points to the photooxidation of NaCl-assisted WS$_2$ after illumination. SHG images of other WS$_2$ and NaCl-assisted WS$_2$ monolayers stored under fluorescent light and 55% RH are shown in Fig. S8† (ESI). We have also put the NaCl-assisted WS$_2$ samples in a Schlenk tube pumped to vacuum (ca. 1.7 × 10^{-3} Torr) and exposed to fluorescent light for 14 days. There is no visible change in the NaCl-assisted WS$_2$ monolayers as shown in Fig. S9† (ESI).

So far, we can draw a conclusion, regardless of the humidity level or the assistance of NaCl, monolayer WS$_2$ is oxidized under light. Light-induced decomposition has been reported in other 2D materials already, such as black phosphorus and InSe, and their degradation is usually involved in the formation of free radicals, such as superoxide ($^{\bullet}$O$_2^-$) and hydroxyl ($^{\bullet}$OH).[49–52] Very recently, the photooxidation effect has been observed and discussed in 2D WS$_2$.[22] Kotsakidis et al.[22] suggested that the oxidation reaction might be Förster resonance energy transfer or photocatalysis involving redox reactions with H$_2$O and O$_2$, and pointed out further study is required. In view of the fact that TMD materials are widely used as photocatalysts for water splitting,[4–6,53] we now consider the potential energy of each energy level in the photocatalytic reaction to clarify the photooxidation of monolayer WS$_2$. The mechanism for water splitting is inducted by light to the TMD base device to produce free radicals as intermediates. Therefore, the formation of these free radicals may be the key to photooxidation. Photocatalysts, such as WS$_2$, absorb photon energy (ca. 2.0 eV or ca. 620 nm for WS$_2$) when the energy is enough to generate electrons and holes (e$^-$ and h$^+$). Based on the photocatalytic properties of 2D materials, the potential energy of the 2H-WS$_2$ conduction band and valence band are located at −3.6 and −5.6 eV vs. vacuum, respectively.[4,5,54] The excited electrons in the conduction band react with O$_2$ forming superoxide ($^{\bullet}$O$_2^-$), where the O$_2$/$^{\bullet}$O$_2^-$ reduction potential energy is −4.1 eV vs. vacuum (see Fig. 3).[49,55,56] The highly
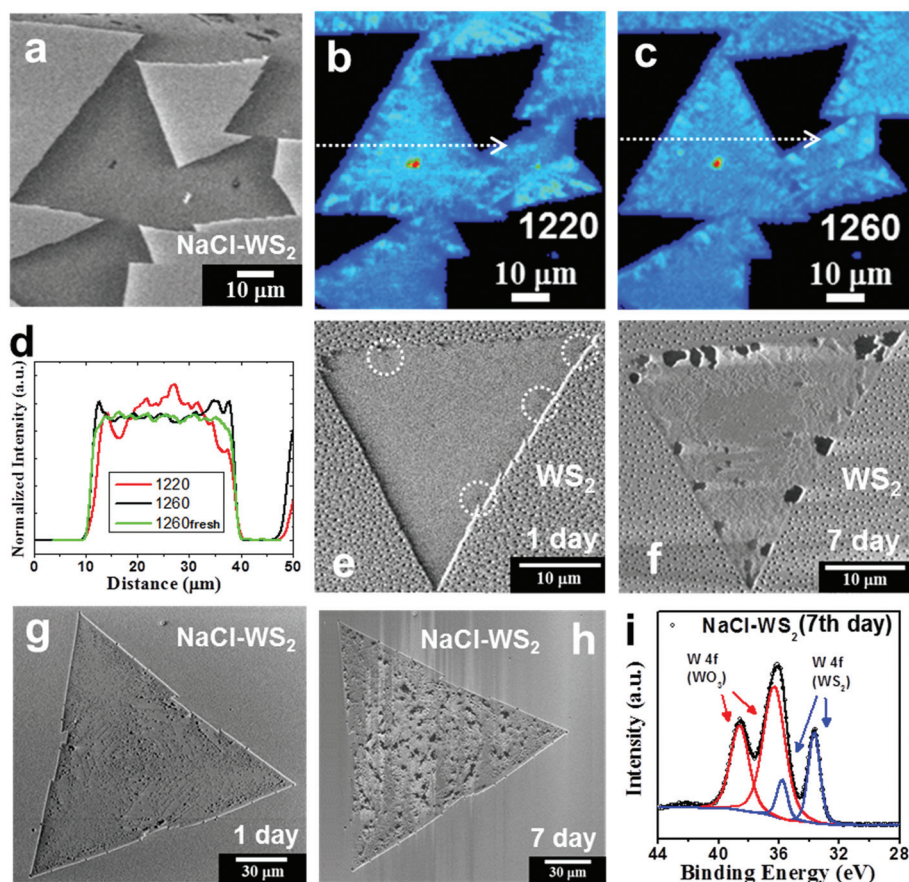
Fig. 2 SHG energy resonance and comparison of photooxidation characteristics of WS$_2$ grown with and without NaCl assistant. (a) SEM image of NaCl-assisted WS$_2$ monolayers stored in a moisture-proof box for 2 months. (b, c) SHG images of the NaCl-assisted WS$_2$ monolayers shown in (a) excited at 1220 and 1260 nm indicating exciton and trion distribution, respectively. The fluence is ~4.6 × 10^7 and 5.1 × 10^7 Jm^{-2}. (d) Intensity profiles measured along the white dotted lines in (b, c) and from the fresh sample shown in Fig. S3b (ESI) with x-axis length shortened for comparison. (e, f) SEM images of a pure WS$_2$ monolayer stored under fluorescent light and 55% RH for 1 day and 7 days, respectively. (g, h) SEM images of a NaCl-assisted WS$_2$ monolayer stored under fluorescent light and 55% RH for 1 day and 7 days, respectively. (i) XPS spectra of the 7th day NaCl-assisted WS$_2$ showing W 4f peaks with Gaussian–Lorentzian fitting.
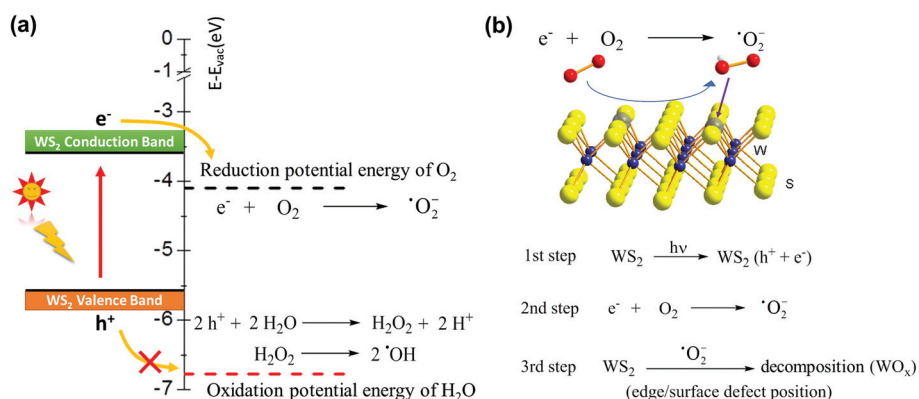

Fig. 3 The photooxidation mechanism of WS$_2$ monolayers. (a) Potential energy referenced to the vacuum level (E-E$_{vac}$) of WS$_2$ conduction band, valence band, reduction potential energy (O$_2$), and oxidation potential energy (H$_2$O). (b) Photoinduction oxidation mechanism for monolayer WS$_2$ with sulfur vacancies (the gray balls position). Step 1: WS$_2$ absorbs photon energy to generate electrons and holes (e$^-$ and h$^+$). Step 2: The conduction band transfers electron to reduce O$_2$ forming ·O$_2^-$. Step 3: Free radicals (superoxide, ·O$_2^-$) attack WS$_2$ from edge or surface sulfur vacancies, where W atoms are exposed and have weak W–S bonds.

reactive free radical ($^{\bullet}O_2^{-}$) then attacks the WS_2 crystal from the edges or surface sulfur vacancies, where metal centers are exposed and have a fragile W–S bond, to undergo oxidation. We also consider the possibility of oxidation *via* a photo-induced H_2O product, which also produces the free radical species ($^{\bullet}OH$). However, the oxidation potential energy is −6.78 eV *vs.* vacuum and H_2O is unable to obtain the energy of the WS_2 valence band, meaning that the oxidation reaction ($H_2O/^{\bullet}OH$) is unlikely to happen (see Fig. 3).[56] Although there are reports that water is necessary for the WS_2 oxidation reaction, the process is not exposed to light or changes little after light exposure.[15,57] For example, WS_2 monolayers stored under moisture-rich conditions at room temperature without light exposure for 1 year went through structural and morphological changes.[15] In another report,[57] after laser irradiation, the WO 4f peaks increased from ∼ 65% to 172% of corresponding WS_2

peak intensities, but the relative intensity of the OH peak increased from ∼ 21.9% to only 29.8% of the main O peak. These are in line with our derivation. We can conclude that $^{\bullet}O_2^{-}$ is the main reactive radical, while $^{\bullet}OH$ plays a minor role in the photooxidation of WS_2.

Next, let us consider the reaction of NaCl-assisted WS_2 in a high-humidity environment that avoids light exposure, and compare it with pure WS_2. Fig. 4a,b show SEM images of pure WS_2 monolayers stored in darkness and 99% RH. The storage time is as indicated. The samples were kept in a double container, where deionized water was dropped between the containers. The outer container was closed carefully to keep moist inside and covered by aluminum foils. The whole set was kept in a metal cabinet to prevent light exposure. The SEM images of the pure WS_2 monolayers show that they are generally stable under this condition (see ESI Fig. S10†), with only some black
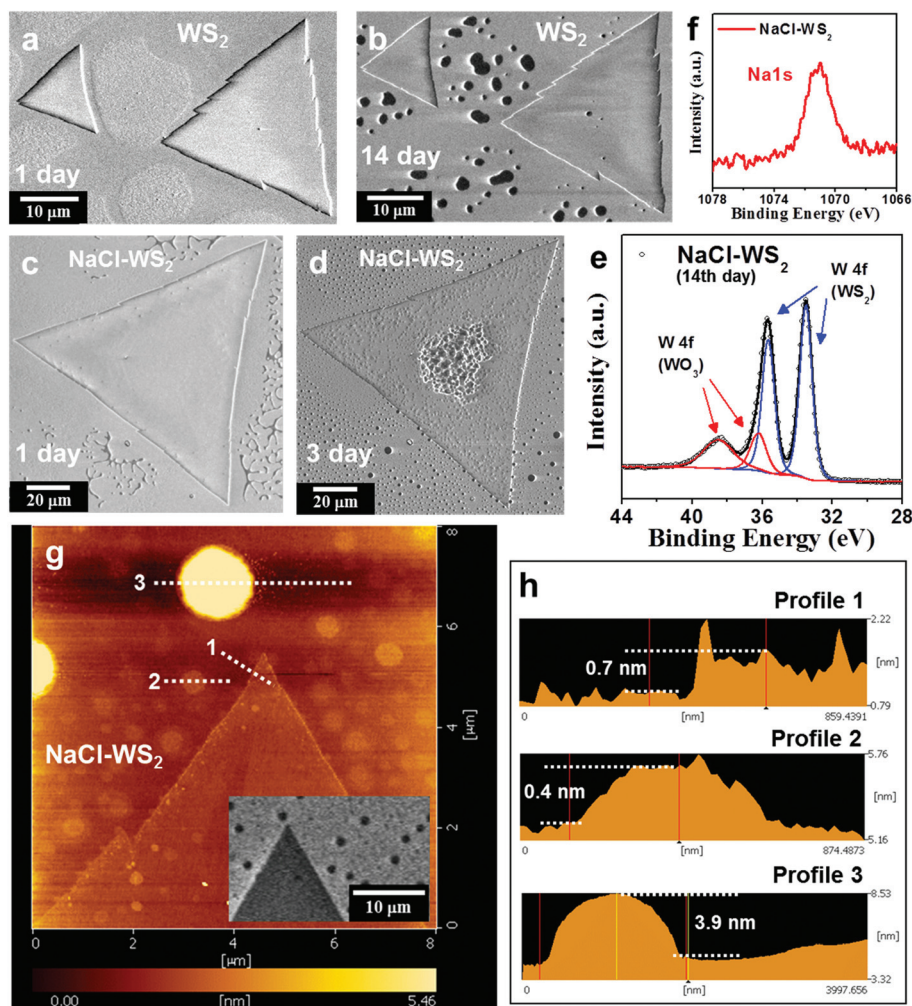

Fig. 4 Comparison of hydrolysis characteristics of WS_2 grown with and without NaCl assistant. (a, b) and (c, d) SEM images of pure and NaCl-assisted WS_2 monolayers stored in darkness and 99% RH, respectively. The storage time is as indicated. There is almost no change in pure WS_2 after 14 days, although the substrate shows a significant difference. Although NaCl-assisted WS_2 after 1 day is not as degraded as the illuminated sample (Fig. 2 g), NaCl-assisted WS_2 after 3 days shows obvious changes. (e) XPS spectra of the 14th day NaCl-assisted WS_2 showing W 4f peaks with Gaussian–Lorentzian fitting. (f) XPS spectra of the Na1s peak from NaCl-assisted WS_2 samples. (g) AFM images of a NaCl-assisted WS_2 monolayer stored in darkness and 99% RH for 3 days. The inset shows its SEM image. (h) The height profile measured along the white dotted lines in (g).

spots appearing on the 14th day, although the substrate has a significant difference, which may be caused by the stoichiometric imbalance of W and S at the crystal nuclei in this area.[58] These results indicate that generally WS$_2$ crystals can tolerate a high-humidity environment without light exposure, agreeing with the DFT prediction made by Zhou et al.[55] Fig. 4c,d show SEM images of NaCl-assisted WS$_2$ monolayers stored in darkness and 99% RH. Although NaCl-assisted WS$_2$ after 1 day is not as degraded as the illuminated one (see Fig. 2g), NaCl-assisted WS$_2$ after 3 days has obvious changes. Interestingly, a blister pattern appears on the center of the NaCl-assisted WS$_2$ triangle beginning on the 3rd day (see ESI Fig. S11†), and this has been found on all NaCl-assisted WS$_2$ crystals in this sample. Fig. 4e shows the XPS spectra of the 14th day NaCl-assisted WS$_2$ showing W 4f peaks with Gaussian–Lorentzian fitting. The W 4f (WO$_3$) signal appears in the XPS spectrum but has a smaller intensity than the W 4f (WS$_2$) peak. Compared with the illuminated NaCl-assisted WS$_2$ (see Fig. 2i), the oxidation degree of NaCl-assisted WS$_2$ in high humidity and darkness is much lower than the degree of the illuminated samples. This means that in a high-humidity and dark environment, in addition to a small amount of WO$_3$, NaCl-assisted WS$_2$ should also generate new products, which are not present in pure WS$_2$. XPS spectra of the NaCl-assisted WS$_2$ samples were collected after the degradation process and showed the presence of Na (see Fig. 4f).[59] It should be noted that the XPS measurement is not sufficient to confirm that Na is in the WS$_2$ lattice, and such Na signals may also come from Na compounds on the substrate.[60] There are some salt-assisted CVD methods that do not find the presence of Na. The researchers used NaCl and WO$_3$ to mix directly and only found that the existence of Cl bonds to other elements.[61] Or use metal sources (e.g. Na$_2$WO$_4$) for the growth of WS$_2$,[62] which is different from placing NaCl and WO$_3$ separately in this study (see Methods). Although spectroscopic evidence alone cannot indicate which sodium intermediates are involved in the CVD process, this is clear evidence that sodium helps crystal growth. In a previous report,[11] the micro-XPS spectra were taken on the early nuclei formed on sapphire substrate and pointed out that volatile Na$_x$WO$_y$ was involved in the growth progress. In this work, the following sulfurization of Na$_x$WO$_y$ nuclei is most likely to generate Na$_x$WS$_2$. The presence of sodium in the XPS spectra shows that sodium interacts with WS$_2$ crystals. In the literature, Na$_x$WS$_2$ is widely studied for sodium ion battery use in order to a gain better performance compared to lithium-ion batteries. The chemical reaction of Na$_x$WS$_2$ in a sodium ion battery anode can be described to the follows:[63]

$$Na_xWS_2 \leftrightarrow xNa^+ + WS_2 + xe^-. \tag{1}$$

The Na$^+$ storage mechanisms within WS$_2$ can be described by the following equation:[64]

$$4Na^+ + WS_2 + 4e^- \rightarrow W + 2Na_2S. \tag{2}$$

The by-product Na$_2$S from eq. 2 then undergoes hydrolysis in a high-humidity and dark environment, reacts with H$_2$O

and forms NaOH and H$_2$S.[65,66] In our case, these are enough to cause the decomposition of the NaCl-assisted WS$_2$ sample, like the blister pattern on the center (see Fig. 4d). Another cause of WS$_2$ surface defects might be chlorides. However, there is no evidence that chloride exists through XPS (see ESI Fig. S12†), so we can exclude the hypothesis of chloride effect.

To study the surface topography of the sample, which is more difficult to be distinguished in SEM and optical methods, we used AFM to image the sample. The AFM image of a NaCl-assisted WS$_2$ monolayer stored under fluorescent light and 55% RH for 1 day is shown in Fig. S13† (ESI). There was a small raised area in the middle of the triangular oxide island, similar to what Kotsakidis et al.[22] report. For the sample stored in darkness and 99% RH for 3 days, as seen in Fig. 4d, black dots appear on both NaCl-assisted WS$_2$ and the sapphire substrate. These look like holes in the SEM image, especially on the substrate. To clarify this, the sample was measured by AFM, shown in Fig. 4 g. The inset shows the SEM image of the same area. Fig. 4 h shows the height profile measured along the white dotted lines in Fig. 4 g. For profile 1, the NaCl-assisted WS$_2$ triangle shows that it has a height of ~0.7 nm, confirming that it is a monolayer WS$_2$. We also observed the raised edges, but the edge width is only ~70 nm, which is smaller than the 0.32 μm width of illuminated WS$_2$.[22] Profiles 2 and 3 confirm that these black dots are not holes but are protrusions in topography. The small and big dots have a height of 0.4 and 3.9 nm and a diameter of 0.52 and 1.56 μm, respectively. We conducted energy-dispersive X-ray spectroscopy (EDS) analysis on the big dot and found the presence of O, Na, W, Al, and S elements (see ESI Fig. S14†).[63,67] This is consistent with the XPS's observation of Na from NaCl-assisted WS$_2$ samples (see Fig. 4f). Compared with W, the content of S and Na is relatively low. Due to the sapphire substrate, the ratio of W to O cannot be obtained correctly. However, it can be inferred that these dots should be mainly WO$_x$.

We found that NaCl-assisted WS$_2$ in a specific orientation has anti-photooxidation properties (see ESI Fig. S15†). Kotsakidis et al.[22] believe that the oxidation on the basal plane begins with sulfur vacancy defects.[15,68] Here, we discuss the use of changing growth conditions to improve the photooxidation effect. Some reports have pointed out that the lattice structures, step edges, and surface interaction of the sapphire substrate will affect the orientation and properties of TMDs.[36–39] Therefore, we intentionally placed the c-plane sapphire in two orientations with respect to the CVD gas flow, and keep the other growth parameters the same. To the purpose of improving photooxidation, we recommend adding less NaCl (~0.5 mg) to the growth of WS$_2$, which still helps to grow larger domains. Fig. 5a shows an optical micrograph of NaCl-assisted WS$_2$ monolayers when the gas flow direction is parallel to the [11$\bar{2}$0] direction of the c-plane sapphire during the growth. We call this WS$_2$ Type I. Most Type I NaCl-assisted WS$_2$ edges are parallel to the [11$\bar{2}$0] direction, as indicated by the yellow dotted lines. In order to confirm the photooxidation tolerance, two Type I NaCl-assisted WS$_2$ flakes were subjected
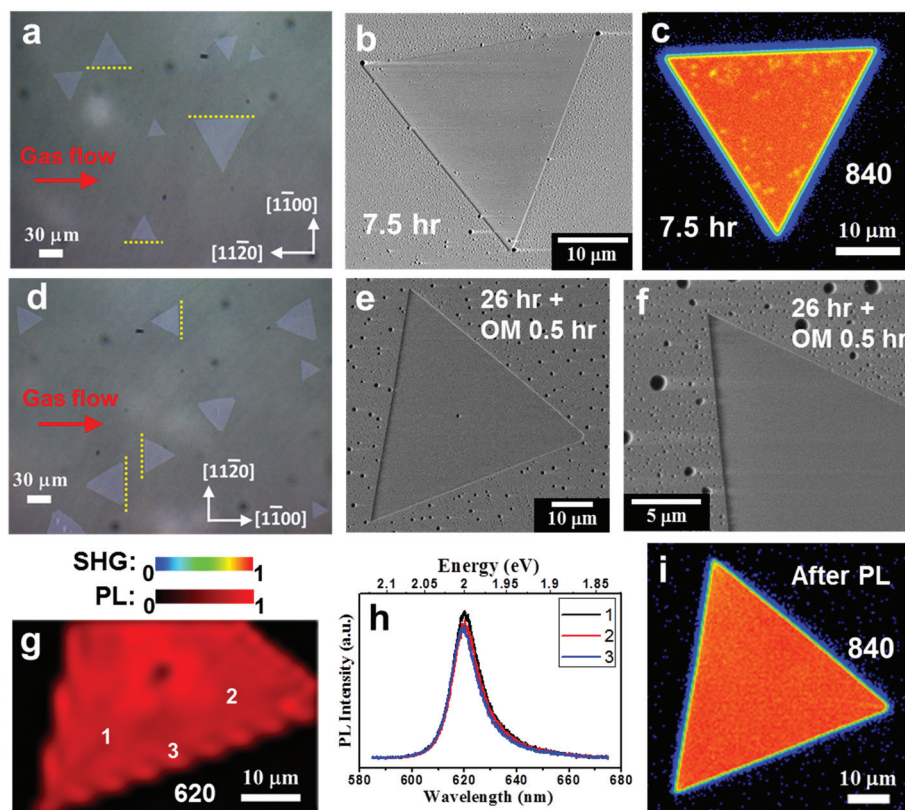
Fig. 5 Changing the orientation of the sapphire substrate during CVD growth to improve the stability of NaCl-assisted WS$_2$. (a) Optical micrograph of NaCl-assisted WS$_2$ monolayers when the gas flow direction is parallel to the [11$\bar{2}$0] direction of c-plane sapphire during the growth (called Type I). Most Type I NaCl-assisted WS$_2$ edges (yellow dotted lines) are parallel to the [11$\bar{2}$0] direction. (b, c) SEM and SHG images of different Type I NaCl-assisted WS$_2$ flakes after 7.5 hours of fluorescent light exposure, respectively. (d) Optical micrograph of NaCl-assisted WS$_2$ monolayers when the gas flow direction is parallel to the [1$\bar{1}$00] direction during the growth (called Type II). (e, f) SEM images of different Type II NaCl-assisted WS$_2$ flakes after 26 hours of fluorescent light and 0.5 hours OM light exposure. There is no appreciable photooxidation characteristic. (g) PL mapping of the same NaCl-assisted WS$_2$ flake as in (e) with laser fluence of ~4.8 × 10^8 Jm^{-2}. (h) Randomly selected PL spectra as marked in (g). (i) SHG image of the same NaCl-assisted WS$_2$ flake as in (e) excited at 840 nm with fluence of ~3.1 × 10^6 Jm^{-2} after light exposure and PL mapping.

to SEM and SHG measurements after 7.5 hours of fluorescent light exposure with fluence of ~4.5 × 10^4 Jm^{-2} at 55% RH, as shown in Fig. 5b,c. Distinguishable oxidation appears in the SEM image, even if the fluence is small. In the SHG image, there are also spots with reduced intensity. More SEM and SHG images of Type I NaCl-assisted WS$_2$ flakes after 7.5 hours of fluorescent light exposure are shown in Fig. S16† (ESI), indicating the photooxidation effect on WS$_2$ grown with 0.5 mg NaCl assistant. Fig. 5d shows an optical micrograph of NaCl-assisted WS$_2$ monolayers when the gas flow direction is parallel to the [1$\bar{1}$00] direction during the growth. We call this WS$_2$ Type II. Most Type II NaCl-assisted WS$_2$ edges are also parallel to the [11$\bar{2}$0] direction, as indicated by the yellow dotted lines. But now the [11$\bar{2}$0] direction of the substrate is perpendicular to the gas flow. Under this condition, we carried out the photooxidation inspection again. After we continued to increase the fluorescent light exposure time to 26 hours and added 0.5 hours of OM exposure with total fluence of ~2.7 × 10^5 Jm^{-2}, there was no appreciable photooxidation characteristic, as shown in Fig. 5e. Fig. 5f shows a high-magnification SEM image of another Type II NaCl-assisted WS$_2$. The NaCl-assisted

WS$_2$ shows a uniform and flawless image. To achieve more stringent and accelerated testing, we performed PL mapping on the same NaCl-assisted WS$_2$ flake in Fig. 5e. The PL intensity map at 620 nm with laser fluence of ~4.8 × 10^8 Jm^{-2} is shown in Fig. 5 g. The PL map shows a very uniform image, except for the nucleus in the center. Randomly selected PL spectra as marked in Fig. 5 g are shown in Fig. 5 h. As we can see, there is a pure exciton peak at 2 eV, and the three PL spectra are similar. This means that Type II NaCl-assisted WS$_2$ can withstand high light fluence without discernible photooxidation. We checked the integrity of the same NaCl-assisted WS$_2$ flake with SHG again and found that it showed no signs of degradation after light exposure and PL mapping (see Fig. 5i).

We try to explain why Type II NaCl-assisted WS$_2$'s photooxidation tolerance can be improved. Based on the above results, we know that this is related to the intrinsic quality of the material. That is, the reduction of sulfur vacancies.[15,22] Although annular dark-field scanning transmission electron microscopy can be used to judge changes in the atomic scale, the scope of its observation is quite limited for the entire WS$_2$.
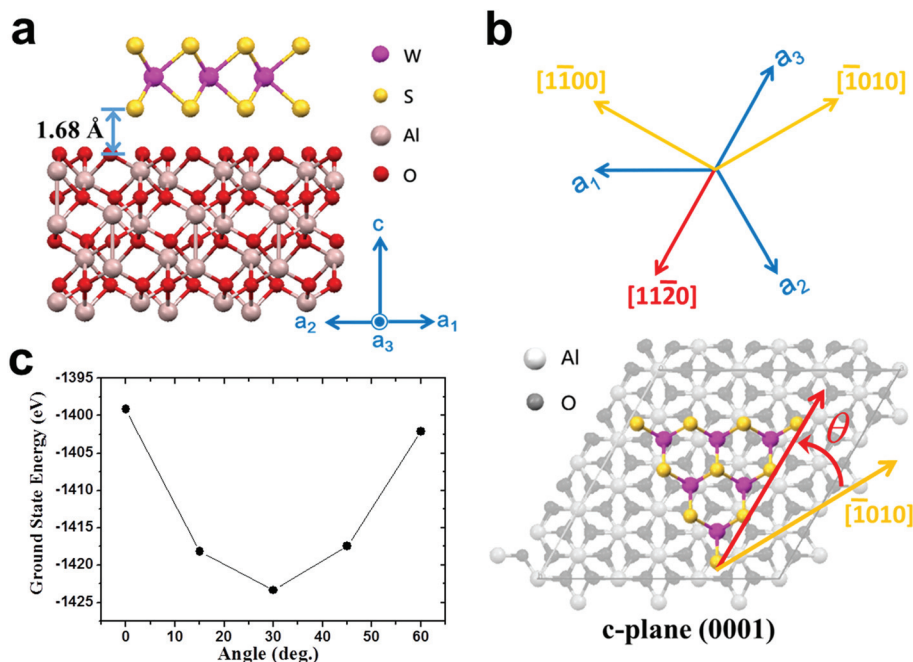
Fig. 6 First-principles DFT calculations of the optimal geometric structure and ground state energy. (a) Atomic model of the DFT calculation. Our calculation results show that the distance between NaCl-assisted WS_2 and sapphire is 1.68 Å. (b) Top view of the atomic model and the definition of the angle θ between NaCl-assisted WS_2 and sapphire. The coordinate axis of the system is also shown. (c) Calculated ground state energy as a function of the angle between NaCl-assisted WS_2 and sapphire.

In addition, atomic damage may be caused during the transfer process or the observation process. Our systematic verification is sufficient to prove the implied sulfur vacancy changes. Therefore, we need to discuss only one change in the growth conditions, which is the orientation of the substrate. First, regardless of the orientation of the substrate, most of NaCl-assisted WS_2 grows along the [11$\bar{2}$0] direction. This is similar to the step-edge-guided growth of aligned WSe_2 on Sapphire.[38] However, the growth temperature of our system is 850 °C, which is lower than the 950 °C indicated in the literature. This means that the sapphire substrate should not produce obvious steps (see ESI Fig. S17†).[69] Here, the optimal geometric structures and ground state energies are investigated by the first-principles DFT using the Vienna *ab initio* simulation package (VASP) (see Methods).[70,71] Our calculation results display an interlayer distance of 1.68 Å, which is close to the previously reported case,[72] and the corresponding ground state energies for 0°, 15°, 30°, 45°, and 60° are, respectively, −1399.13, −1418.16, −1423.35, −1417.48, and −1402.09 eV (see Fig. 6). The results show that compared with other cases, the 30° case is relatively more stable, whose edges are parallel to the sapphire [11$\bar{2}$0] direction. The calculation results explain the growth orientation of WS_2. However, this is still not sufficient to explain the quality difference between Type I and Type II NaCl-assisted WS_2. Secondly, it has been reported that simulating the growth of CVD MoS_2 by considering concentrations and concentration gradients of precursors and carrier gas stream velocities is a viable option.[73,74] However, the authors used SiO_2/Si as the substrate and did not consider single

crystal substrates, such as sapphire.[73,74] The atomic structure properties of the substrate play a crucial role in the nucleation, growth, and orientation of TMDs. Combining transport behavior and substrate interaction is a complex process, and we do not have the ability to perform such simulations. Please note that these novel experimental results are not fully matched by our DFT-based calculations, which call for more sophisticated simulations based on a multiscale model.[73] From the report of Momeni *et al.*,[73] it is known that the growth directions of the MoS_2 triangle tips are affected by the precursor concentration distribution and gas flow direction. According to the orientation and symmetry of WS_2 in this study, we can expect that NaCl-assisted WS_2 will have a better growth quality when the gas flow direction is perpendicular to the [11$\bar{2}$0] direction. This contributes to the nucleation and subsequent growth of NaCl-assisted WS_2. In fact, this can be proven by the experimental results. Type II NaCl-assisted WS_2 has a higher growth density, and its average grain size is 56 μm, which is larger than the Type I NaCl-assisted WS_2's 37 μm (see ESI Fig. S18 and S19†).

Conclusions

We have demonstrated second-harmonic imaging microscopy as a fast, non-photooxidative damage and energy characteristic technology for WS_2 monolayers. This is because the exciton 1*s* transition is dipole forbidden in two-photon absorption but is allowed in SHG. Photooxidation occurs only when a real elec-

tronic transition is excited. With this technology, we can explore the oxidation and degradation mechanisms of WS_2 in its original state. The function of NaCl assistant affects the grain size and results in larger monolayer WS_2 crystals in CVD fabrication. However, using NaCl has its disadvantages too, which results in a higher sensitivity of the WS_2 crystals to moisture. We use a photocatalytic reaction to explain the photo-induced oxidation mechanism of monolayer WS_2 with sulfur vacancies. It is concluded that $^\bullet O_2^-$ is the main reactive radical, while $^\bullet OH$ plays a minor role in the photooxidation of WS_2. When not exposed to light, pure WS_2 crystals can tolerate in a high-humidity environment, but NaCl-assisted WS_2 generates new products under this condition. The XPS spectra of NaCl-assisted WS_2 samples collected after the degradation process show the presence of Na but no Cl. Finally, we discuss the use of changing growth conditions to improve the photooxidation properties of NaCl-assisted WS_2. We intentionally placed the c-plane sapphire in two orientations with respect to the CVD gas flow and kept the other growth parameters the same. According to the orientation and symmetry of NaCl-assisted WS_2, we can expect that it will have a better growth quality when the gas flow direction is perpendicular to the [11$\bar{2}$0] direction of sapphire substrate. This contributes to the nucleation and subsequent growth of NaCl-assisted WS_2. The DFT-based calculations can explain the growth orientation of WS_2. This growth method can greatly improve the stability of NaCl-assisted WS_2 in the ambient atmosphere, even when exposed to light with fluence greater than 4.8×10^8 Jm^{-2}. This research provides a more stable measurement method than laser scanning confocal microscopy and fluorescence microscopy, namely SHG, and greatly improves the operational stability of NaCl-assisted WS_2 under environmental conditions.

Methods

CVD Monolayer NaCl-Assisted WS_2 Growth

Tungsten(VI) oxide (WO_3, 99.8%) and elemental sulfur powder (99.8% and 99.98%) were obtained from Sigma-Aldrich. NaCl was purchased from Uniregion bio-tech. Sapphire (2 inches sheets, 0.43 mm thickness) substrates (Al_2O_3) were obtained from Crystalwise Technology Inc and cut into 5×5 mm^2 square tiles. The sapphire substrates were washed in an ultrasonicator with acetone, isopropyl alcohol and then deionised water before washing with piranha solution (96% H_2SO_4 and 30% H_2O_2 in 1 : 1 volume ratio), each solvent for 2 minutes. The washed sapphire substrates were rinsed with deionised water and then dried by a N_2 airgun flow. WS_2 monolayers were grown using a typical CVD method (see ESI Fig. S2†). Sapphire substrate and tungsten oxide (WO_3, 300 mg) were placed in the center of the CVD furnace. A mixture (99.8%, 250 mg and 99.98%, 250 mg) of elemental sulfur powder and NaCl (1 mg, option, see discussion for detail) were placed at the upstream side of the furnace at carefully adjusted location in order to set the temperature. The temperature of the

furnace was raised to 850 °C. The sulfur precursor and NaCl grains were kept at ~175 °C and ~600 °C, respectively. The growth time was 20 min with argon (200 sccm) and H_2 (15 sccm) constantly flowing through the tube and under 20 Torr working pressures. The furnace was cooled down to room temperature naturally.

Characterization

SEM images were collected using a JEOL JSM7000 with an accelerating voltage of 5 kV. Raman spectra were collected by a Thermo Scientific DXR Raman Microscope with a Nd:YAG 532 nm laser, and the power on the sample is about 0.1 mW. The micro-PL studies were conducted using a Renishaw inVia confocal system excited with a Cobolt 514.5 nm diode-pumped solid-state laser for all WS_2 PL spectra through a 50× objective of a Leica microscope at room temperature and equipped with a thermoelectrically cooled detector. The spot diameter was about 0.7 μm. For the PL measurements, the laser power was shown in the text. For PL mapping, the sample was moved by a motorised stage in the x and y directions with scan step size of 1.5 μm. The topographies of the WS_2 monolayers were characterized using the tapping mode of a Bruker Dimension Icon AFM. XPS data were obtained from a ULVAC-PHI Quantera II and calibrated using carbon C1s peak.

Second-Harmonic Generation Measurements

SHG measurements were performed using an in-house multiphoton laser scanning microscope. The fundamental laser field was provided by a mode-locked Ti:sapphire laser and an optical parametric oscillator at a fundamental wavelength of 680–1600 nm with a pulse width of 140–200 fs and a repetition rate of 80 MHz. The laser pulse was focused on the sample by a 20×0.8NA plan apochromat objective. The laser beam was scanned with a 2D galvo mirror system. The backscattered second-harmonic emission generated from the TMD monolayers passed through a short-pass dichroic mirror (cut-off at 670 nm for laser wavelength <1000 nm or cut-off at 875 nm for laser wavelength >1000 nm), and was divided into four channels using three dichroic mirrors and one mirror. The second-harmonic light was detected using four photomultiplier tubes accompanied with band-pass filters to suppress signals from different bands.

DFT Calculations

The exchange–correlation due to the electron–electron interactions is calculated from the Perdew–Burke–Ernzerhof functional under the generalized gradient approximation (GGA).[75] The van der Waals interaction is employed in the calculations using the Grimme correlation to correctly describe the significant atomic interactions between layered WS_2 and the sapphire. Furthermore, the convergence condition of the ground state energy is set to be $\sim 10^{-5}$ eV between two consecutive evaluation steps. The optimized geometric calculations are started from WS_2 and the sapphire (Al_2O_3) slab consisting of 3 × 3 unit cells with 4 layers of oxides. The interlayer distance between WS_2 and sapphire slab is set to be 1.65 Å according to

the previous work and allowed to be changed by computational system.[72] Based on computational load considerations, optimized structures and energy calculations are utilized with $2 \times 2 \times 2$ k points within the Monkhorst–Pack grid.[76] We calculate the ground state energies of five different rotational degrees of WS_2 on sapphire, which includes 0°, 15°, 30°, 45°, and 60°.

Data availability

The data that support the findings of this study are available from the corresponding author upon reasonable request.

Author contributions

K.-I.L. and P.-W.C. conceived the concept and experiment. Y.-P. C., Y.-C.Y. and H.-L.L. performed the growth and SEM measurements. Y.-P.C. carried out the AFM, XPS, Raman and PL characterizations. K.-I.L. performed the SHG and PL measurements. W.-B.L. and M.-F.L. carried out the theoretical calculations. K.-I.L. and Y.-P.C. wrote the paper. All authors discussed the results and commented on the manuscript at all stages.

Conflicts of interest

The authors declare that there are no competing interests.

Acknowledgements

References

1 J. Feng, X. Sun, C. Wu, L. Peng, C. Lin, S. Hu, J. Yang and Y. Xie, *J. Am. Chem. Soc.*, 2011, **133**, 17832–17838.

2 J. Wang, J. Liu, B. Zhang, X. Ji, K. Xu, C. Chen, L. Miao and J. Jiang, *Phys. Chem. Chem. Phys.*, 2017, **19**, 10125–10132.

3 L. Wang and J. B. Sambur, *Nano Lett.*, 2019, **19**, 2960–2967.

4 P. Atkin, T. Daeneke, Y. Wang, B. Carey, K. Berean, R. Clark, J. Ou, A. Trinchi, I. Cole and K. Kalantar-Zadeh, *J. Mater. Chem. A*, 2016, **4**, 13563–13571.

5 Y. Li, Y.-L. Li, B. Sa and R. Ahuja, *Catal. Sci. Technol.*, 2017, **7**, 545–559.

6 G. Koyyada, S. P. Vattikuti, S. Shome, J. Shim, V. Chitturi and J. H. Jung, *Mater. Res. Bull.*, 2019, **109**, 246–254.

7 J. Pu, Y. Yomogida, K.-K. Liu, L.-J. Li, Y. Iwasa and T. Takenobu, *Nano Lett.*, 2012, **12**, 4013–4017.

8 K. Lee, R. Gatensby, N. McEvoy, T. Hallam and G. S. Duesberg, *Adv. Mater.*, 2013, **25**, 6699–6702.

9 Z. Lin, B. R. Carvalho, E. Kahn, R. Lv, R. Rao, H. Terrones, M. A. Pimenta and M. Terrones, *2D Mater.*, 2016, **3**, 022002.

10 Y. C. Lin, S. Li, H. P. Komsa, L. J. Chang, A. V. Krasheninnikov, G. Eda and K. Suenaga, *Adv. Funct. Mater.*, 2018, **28**, 1704210.

11 Y.-C. Lin, C.-H. Yeh, H.-C. Lin, M.-D. Siao, Z. Liu, H. Nakajima, T. Okazaki, M.-Y. Chou, K. Suenaga and P.-W. Chiu, *ACS Nano*, 2018, **12**, 12080–12088.

12 Z. Cai, B. Liu, X. Zou and H.-M. Cheng, *Chem. Rev.*, 2018, **118**, 6091–6133.

13 H.-P. Komsa, J. Kotakoski, S. Kurasch, O. Lehtinen, U. Kaiser and A. V. Krasheninnikov, *Phys. Rev. Lett.*, 2012, **109**, 035503.

14 R. Zan, Q. M. Ramasse, R. Jalil, T. Georgiou, U. Bangert and K. S. Novoselov, *ACS Nano*, 2013, **7**, 10167–10174.

15 J. Gao, B. Li, J. Tan, P. Chow, T.-M. Lu and N. Koratkar, *ACS Nano*, 2016, **10**, 2628–2635.

16 Y. Rong, K. He, M. Pacios, A. W. Robertson, H. Bhaskaran and J. H. Warner, *ACS Nano*, 2015, **9**, 3695–3703.

17 A. Castellanos-Gomez, M. Barkelid, A. Goossens, V. E. Calado, H. S. van der Zant and G. A. Steele, *Nano Lett.*, 2012, **12**, 3187–3192.

18 Z. He, X. Wang, W. Xu, Y. Zhou, Y. Sheng, Y. Rong, J. M. Smith and J. H. Warner, *ACS Nano*, 2016, **10**, 5847–5855.

19 W. Zhang, Z. Huang, W. Zhang and Y. Li, *Nano Res.*, 2014, **7**, 1731–1737.

20 L. Yuan and L. Huang, *Nanoscale*, 2015, **7**, 7402–7408.

21 Q. Zhang, J. Lu, Z. Wang, Z. Dai, Y. Zhang, F. Huang, Q. Bao, W. Duan, M. S. Fuhrer and C. Zheng, *Adv. Opt. Mater.*, 2018, **6**, 1701347.

22 J. C. Kotsakidis, Q. Zhang, A. L. Vazquez de Parga, M. Currie, K. Helmerson, D. K. Gaskill and M. S. Fuhrer, *Nano Lett.*, 2019, **19**, 5205–5215.

23 H. Liu, J. Lu, K. Ho, Z. Hu, Z. Dang, A. Carvalho, H. R. Tan, E. S. Tok and C. H. Sow, *Nano Lett.*, 2016, **16**, 5559–5567.

24 G. Wang, X. Marie, I. Gerber, T. Amand, D. Lagarde, L. Bouet, M. Vidal, A. Balocchi and B. Urbaszek, *Phys. Rev. Lett.*, 2015, **114**, 097403.

25 G. Wang, I. Gerber, L. Bouet, D. Lagarde, A. Balocchi, M. Vidal, T. Amand, X. Marie and B. Urbaszek, *2D Mater.*, 2015, **2**, 045005.

26 J. Xiao, Z. Ye, Y. Wang, H. Zhu, Y. Wang and X. Zhang, *Light Sci. Appl.*, 2015, **4**, e366.

27 K.-I. Lin, S.-Y. Shiau, S.-B. Liu, J.-S. Yan, J.-D. Yan, D. Cheng, H.-C. Chang, C.-L. Tu, Y.-C. Cheng and C.-H. Chen, *J. Phys. Chem. C*, 2020, **124**, 7979–7987.

28 S. Ahn, G. Kim, P. K. Nayak, S. I. Yoon, H. Lim, H.-J. Shin and H. S. Shin, *ACS Nano*, 2016, **10**, 8973–8979.

29 S.-Y. Kim, J. Kwak, J. H. Kim, J.-U. Lee, Y. Jo, S. Y. Kim, H. Cheong, Z. Lee and S.-Y. Kwon, *2D Mater.*, 2016, **4**, 011007.

30 R. Canton-Vitoria, Y. Sayed-Ahmad-Baraza, B. Humbert, R. Arenal, C. P. Ewels and N. Tagmatarchis, *Nanomaterials*, 2020, **10**, 363.

31 J. D. Wood, S. A. Wells, D. Jariwala, K.-S. Chen, E. Cho, V. K. Sangwan, X. Liu, L. J. Lauhon, T. J. Marks and M. C. Hersam, *Nano Lett.*, 2014, **14**, 6964–6970.

32 K. Zhang, B. M. Bersch, F. Zhang, N. C. Briggs, S. Subramanian, K. Xu, M. Chubarov, K. Wang, J. O. Lerach and J. M. Redwing, *ACS Appl. Mater. Interfaces*, 2018, **10**, 40831–40837.

33 Y. Xie, X. Ma, Z. Wang, T. Nan, R. Wu, P. Zhang, H. Wang, Y. Wang, Y. Zhan and Y. Hao, *MRS Adv.*, 2018, **3**, 365–371.

34 S. Li, S. Wang, D.-M. Tang, W. Zhao, H. Xu, L. Chu, Y. Bando, D. Golberg and G. Eda, *Appl. Mater. Today*, 2015, **1**, 60–66.

35 W. Wang, H. Shu, J. Wang, Y. Cheng, P. Liang and X. Chen, *ACS Appl. Mater. Interfaces*, 2020, **12**, 9563–9571.

36 A. Aljarb, Z. Cao, H.-L. Tang, J.-K. Huang, M. Li, W. Hu, L. Cavallo and L.-J. Li, *ACS Nano*, 2017, **11**, 9215–9222.

37 K. Suenaga, H. G. Ji, Y.-C. Lin, T. Vincent, M. Maruyama, A. S. Aji, Y. Shiratsuchi, D. Ding, K. Kawahara and S. Okada, *ACS Nano*, 2018, **12**, 10032–10044.

38 L. Chen, B. Liu, M. Ge, Y. Ma, A. N. Abbas and C. Zhou, *ACS Nano*, 2015, **9**, 8368–8375.

39 H. G. Ji, Y.-C. Lin, K. Nagashio, M. Maruyama, P. Solís-Fernández, A. Sukma Aji, V. Panchal, S. Okada, K. Suenaga and H. Ago, *Chem. Mater.*, 2018, **30**, 403–411.

40 F. Reale, P. Palczynski, I. Amit, G. F. Jones, J. D. Mehew, A. Bacon, N. Ni, P. C. Sherrell, S. Agnoli and M. F. Craciun, *Sci. Rep.*, 2017, **7**, 14911.

41 J. Zhou, J. Lin, X. Huang, Y. Zhou, Y. Chen, J. Xia, H. Wang, Y. Xie, H. Yu and J. Lei, *Nature*, 2018, **556**, 355–359.

42 Y. Li, Y. Rao, K. F. Mak, Y. You, S. Wang, C. R. Dean and T. F. Heinz, *Nano Lett.*, 2013, **13**, 3329–3333.

43 W. Wu, L. Wang, Y. Li, F. Zhang, L. Lin, S. Niu, D. Chenet, X. Zhang, Y. Hao and T. F. Heinz, *Nature*, 2014, **514**, 470–474.

44 M. S. Kim, S. J. Yun, Y. Lee, C. Seo, G. H. Han, K. K. Kim, Y. H. Lee and J. Kim, *ACS Nano*, 2016, **10**, 2399–2405.

45 J. Park, M. S. Kim, E. Cha, J. Kim and W. Choi, *Sci. Rep.*, 2017, **7**, 16121.

46 D. Kozawa, R. Kumar, A. Carvalho, K. K. Amara, W. Zhao, S. Wang, M. Toh, R. M. Ribeiro, A. C. Neto and K. Matsuda, *Nat. Commun.*, 2014, **5**, 4543.

47 K. Kang, K. Godin, Y. D. Kim, S. Fu, W. Cha, J. Hone and E. H. Yang, *Adv. Mater.*, 2017, **29**, 1603898.

48 Y.-C. Lin, T. Björkman, H.-P. Komsa, P.-Y. Teng, C.-H. Yeh, F.-S. Huang, K.-H. Lin, J. Jadczak, Y.-S. Huang and P.-W. Chiu, *Nat. Commun.*, 2015, **6**, 6736.

49 Q. Zhou, Q. Chen, Y. Tong and J. Wang, *Angew. Chem., Int. Ed.*, 2016, **55**, 11437–11441.

50 A. Favron, E. Gaufrès, F. Fossard, A.-L. Phaneuf-L'Heureux, N. Y. Tang, P. L. Lévesque, A. Loiseau, R. Leonelli, S. Francoeur and R. Martel, *Nat. Mater.*, 2015, **14**, 826–832.

51 L. Shi, Q. Zhou, Y. Zhao, Y. Ouyang, C. Ling, Q. Li and J. Wang, *J. Phys. Chem. Lett.*, 2017, **8**, 4368–4373.

52 A. A. Kistanov, Y. Cai, K. Zhou, S. V. Dmitriev and Y.-W. Zhang, *J. Mater. Chem. C*, 2018, **6**, 518–525.

53 C. Byrne, G. Subramanian and S. C. Pillai, *J. Environ. Chem. Eng.*, 2018, **6**, 3531–3555.

54 B. Mahler, V. Hoepfner, K. Liao and G. A. Ozin, *J. Am. Chem. Soc.*, 2014, **136**, 14121–14127.

55 C. Zhou, W. Yang and H. Zhu, *J. Chem. Phys.*, 2015, **142**, 214704.

56 M. Han, L. Hu, Y. Zhou, S. Zhao, L. Bai, Y. Sun, H. Huang, Y. Liu and Z. Kang, *Catal. Sci. Technol.*, 2018, **8**, 840–846.

57 P. Atkin, D. Lau, Q. Zhang, C. Zheng, K. Berean, M. Field, J. Ou, I. Cole, T. Daeneke and K. Kalantar-Zadeh, *2D Mater.*, 2018, **5**, 015013.

58 S. Wang, Y. Rong, Y. Fan, M. Pacios, H. Bhaskaran, K. He and J. H. Warner, *Chem. Mater.*, 2014, **26**, 6371–6379.

59 H. Kim, D. Ovchinnikov, D. Deiana, D. Unuchek and A. Kis, *Nano Lett.*, 2017, **17**, 5056–5063.

60 Z. Cai, T. Shen, Q. Zhu, S. Feng, Q. Yu, J. Liu, L. Tang, Y. Zhao, J. Wang, B. Liu and H.-M. Cheng, *Small*, 2020, **16**, 1903181.

61 J. Zhou, J. Lin, X. Huang, Y. Zhou, Y. Chen, J. Xia, H. Wang, Y. Xie, H. Yu and J. Lei, *Nature*, 2018, **556**, 355–359.

62 Z. Cai, Y. Lai, S. Zhao, R. Zhang, J. Tan, S. Feng, J. Zou, L. Tang, J. Lin, B. Liu and H.-M. Cheng, *Natl. Sci. Rev.*, 2021, **8**, nwaa115.

63 Y. Von Lim, Y. Wang, D. Kong, L. Guo, J. I. Wong, L. Ang and H. Y. Yang, *J. Mater. Chem. A*, 2017, **5**, 10406–10415.

64 S. H. Choi and Y. C. Kang, *Nanoscale*, 2015, **7**, 3965–3970.

65 C. S. Cucinotta, K. Dolui, H. Pettersson, Q. M. Ramasse, E. Long, S. E. O'Brian, V. Nicolosi and S. Sanvito, *J. Phys. Chem. C*, 2015, **119**, 15707–15715.

66 E. Sminčáková and Ľ. Komorová, *Annals of Faculty of Engineering Hunedoara-Journal of Engineering VI*, 2008, **1**, 17–24.

67 S. Rostami, S. N. Azizi and S. Ghasemi, *J. Electroanal. Chem.*, 2017, **788**, 235–245.

68 M. Zhang, M. Lihter, T.-H. Chen, M. Macha, A. Rayabharam, K. Banjac, Y. Zhao, Z. Wang, J. Zhang and J. Comtet, *ACS Nano*, 2021, **15**, 7168–7178.

69 S. Curiotto and D. Chatain, *Appl. Surf. Sci.*, 2009, **603**, 2688–2697.

70 G. Kresse and D. Joubert, *Phys. Rev. B*, 1999, **59**, 1758–1775.

71 G. Kresse and J. Furthmüller, *Comput. Mater. Sci.*, 1996, **6**, 15–50.

72 H. G. Ji, M. Maruyama, A. S. Aji, S. Okada, K. Matsuda and H. Ago, *Phys. Chem. Chem. Phys.*, 2018, **20**, 29790–29797.

73 K. Momeni, Y. Ji, K. Zhang, J. A. Robinson and L.-Q. Chen, *NPJ 2D Mater Appl*, 2018, **2**, 27.

74 F. Zhang, K. Momeni, M. A. AlSaud, A. Azizi, M. F. Hainey, J. M. Redwing, L.-Q. Chen and N. Alem, *2D Mater.*, 2017, **4**, 025029.

75 J. P. Perdew, K. Burke and M. Ernzerhof, *Phys. Rev. Lett.*, 1996, **77**, 3865–3868.

76 H. J. Monkhorst and J. D. Pack, *Phys. Rev. B*, 1976, **13**, 5188–5192.